The Soft-Excess in Mrk 509: Warm Corona or Relativistic Reflection?

Javier A. García,[1,2] Erin Kara,[3] Dominic Walton,[4] Tobias Beuchert,[5] Thomas Dauser,[2] Efrain Gatuzz,[6,7] Mislav Balokovic,[8] James F. Steiner,[9] Francesco Tombesi,[10,11,12,3] Riley M. T. Connors,[1] Timothy R. Kallman,[12] Fiona A. Harrison,[1] Andrew Fabian,[4] Jörn Wilms,[2] Daniel Stern,[13] Lauranne Lanz,[14] Claudio Ricci,[15,16,17] and David R. Ballantyne[18]

[1]Cahill Center for Astronomy and Astrophysics, California Institute of Technology, Pasadena, CA 91125, USA

[2]Dr. Karl Remeis-Observatory and Erlangen Centre for Astroparticle Physics, Sternwartstr. 7, 96049 Bamberg, Germany

[3]Department of Astronomy, University of Maryland, College Park, MD 20742, USA

[4]Institute of Astronomy, Madingley Road, Cambridge CB3 0HA, UK

[5]Anton Pannekoek Institute for Astronomy, Universiteit van Amsterdam, Science Park 904, 1098 XH, Amsterdam, The Netherlands

[6]ESO, Karl-Schwarzschild-Strasse 2, D-85748 Garching bei München, Germany

[7]Excellence Cluster Universe, Boltzmannstr. 2, D-85748, Garching, Germany

[8]Harvard-Smithsonian Center for Astrophysics, 60 Garden Street, Cambridge, MA 02140, USA

[9]MIT Kavli Institute for Astrophysics and Space Research, MIT, 70 Vassar Street, Cambridge, MA 02139

[10]Dipartimento di Fisica, Università di Roma "Tor Vergata", via della Ricerca Scientifica 1, I-00133, Roma, Italy

[11]INAF Astronomical Observatory of Rome, Via Frascati 33, 00078 Monteporzio Catone, Italy

[12]NASA/Goddard Space Flight Center, Code 662, Greenbelt, MD 20771, USA

[13]Jet Propulsion Laboratory, California Institute of Technology, 4800 Oak Grove Drive, Mail Stop 169-221, Pasadena, CA 91109, USA

[14]Department of Physics and Astronomy, Dartmouth College, 6127 Wilder Laboratory, Hanover, NH 03755, USA

[15]Núcleo de Astronomía de la Facultad de Ingeniería, Universidad Diego Portales, Av. Ejército Libertador 441, Santiago, Chile

[16]Kavli Institute for Astronomy and Astrophysics, Peking University, Beijing 100871, China

[17]Chinese Academy of Sciences South America Center for Astronomy, Camino El Observatorio 1515, Las Condes, Santiago, Chile

[18]Center for Relativistic Astrophysics, School of Physics, Georgia Institute of Technology, 837 State Street, Atlanta, GA 30332-0430

ABSTRACT

We present the analysis of the first *NuSTAR* observations ($\sim 220\,$ks), simultaneous with the last *Suzaku* observations ($\sim 50\,$ks), of the active galactic nucleus of the bright Seyfert 1 galaxy Mrk 509. The time-averaged spectrum in the $1 - 79\,$keV X-ray band is dominated by a power-law continuum ($\Gamma \sim 1.8 - 1.9$), a strong soft excess around $1\,$keV, and signatures of X-ray reflection in the form of Fe K emission ($\sim 6.4\,$keV), an Fe K absorption edge ($\sim 7.1\,$keV), and a Compton hump due to electron scattering ($\sim 20 - 30\,$keV). We show that these data can be described by two very different prescriptions for the soft excess: a warm ($kT \sim 0.5 - 1\,$keV) and optically thick ($\tau \sim 10 - 20$) Comptonizing corona, or a relativistically blurred ionized reflection spectrum from the inner regions of the accretion disk. While these two scenarios cannot be distinguished based on their fit statistics, we argue that the parameters required by the warm corona model are physically incompatible with the conditions of standard coronae. Detailed photoionization calculations show that even in the most favorable conditions, the warm corona should produce strong absorption in the observed spectrum. On the other hand, while the relativistic reflection model provides a satisfactory description of the data, it also requires extreme parameters, such as maximum black hole spin, a very low and compact hot corona, and a very high density for the inner accretion disk. Deeper observations of this source are thus necessary to confirm the presence of relativistic reflection, and to further understand the nature of its soft excess.

Corresponding author: Javier A. García
javier@caltech.edu

1. INTRODUCTION

Accretion onto supermassive black holes in active galactic nuclei (AGN) is one of the most efficient mechanisms to convert gravitational energy into radiation, comprised mostly of very energetic photons. For this reason, X-ray spectroscopy is a resourceful technique to study supermassive black holes and their interaction with their surroundings. In the case of most Seyfert AGN, the X-ray continuum is typically dominated by a power-law that extends to high energies, which is thought to be produced either in a central hot corona (e.g., Shakura & Sunyaev 1973; Haardt 1993), or at the base of a jet (e.g., Matt et al. 1992; Markoff et al. 2005), although the exact mechanism is still a matter of study. Thermal emission from the accretion disk peaks in the ultraviolet (UV) band, extending partially to the soft X-rays. A fraction of the coronal emission illuminates the accretion disk, producing a rich reflection spectrum of fluorescent lines and other spectral features. This reflection component can be ionized, as changes in the ionization state of the disk determine spectral features observed (e.g., Ross & Fabian 2005; García & Kallman 2010), and also blurred and distorted by relativistic effects (e.g., Laor 1991; Crummy et al. 2006), if it originates close enough to the supermassive black hole; or it can be cold and neutral, if produced farther from the black hole in either the broad-line region or the torus (e.g., Matt et al. 1991; George & Fabian 1991).

In a large fraction of Seyfert AGN a soft excess component is also observed peaking near 1–2 keV. Its origin has been debated over the years. This soft excess was first believed to be the hard tail of UV blackbody emission from the accretion disk (Singh et al. 1985; Arnaud et al. 1985; Pounds et al. 1986; Magdziarz et al. 1998; Leighly 1999); however, this explanation was ruled out given that systems with very different accretion rates and/or masses would be characterized by the same blackbody temperature, which is not expected for an accretion disk (Gierliński & Done 2004; Porquet et al. 2004; Piconcelli et al. 2005; Miniutti et al. 2009). The current models invoked to explain the soft excess tend to favor either Comptonization of UV photons or blurred ionized reflection. In the first case, the disk photons are Comptonized by a corona above the disk, which is optically thicker and cooler than the corona responsible for the primary X-ray emission (Czerny & Elvis 1987; Middleton et al. 2009; Jin et al. 2009; Done et al. 2012). In the second case, the emission lines produced in the disk are relativistically blurred due to the proximity to the black hole (Fabian et al. 2002; Ross & Fabian 2005; Crummy et al. 2006; García & Kallman 2010; Walton et al. 2013).

The Seyfert type 1 galaxy Mrk 509 was one of the first AGN to be studied in detail because it is luminous ($L_{Bol} = 1.07 \times 10^{45}$ erg s^{-1}; Woo & Urry 2002) and relatively nearby ($z = 0.0344$; Fisher et al. 1995). The corresponding X-ray flux of $F_x = (2$–$5) \times 10^{-11}$ erg cm^{-2} s^{-1} (Kaastra et al. 2011) is powered by a $1.4 \times 10^8 M_\odot$ black hole (Peterson et al. 2004), which is accreting at 20–30% of the Eddington rate (Petrucci et al. 2013). Excess soft ($\lesssim 2$ keV) emission above the extrapolation of the hard X-ray continuum was first identified by Singh et al. (1985). After Morini et al. (1987) detected the Fe line, improved X-ray instruments and detectors led to a full discussion of reflection features by Pounds et al. (1994).

An intense campaign of multi-wavelength monitoring of Mrk 509 involving the X-ray observatories *XMM-Newton* and *Suzaku* has provided a detailed model for the observed set of soft-X-ray absorption features, caused by differentially ionized warm absorbing gas (Kaastra et al. 2011). Portions of this gas phase have been observed to be outflowing at different velocities (Smith et al. 2007), including a component classed as an ultra-high velocity outflow (Cappi et al. 2009). This campaign also resulted in the most complete study of the Fe K complex of Mrk 509 to date, revealing a neutral narrow component and an ionized broad component. The latter has been interpreted as relativistic reflection from the inner regions of the accretion disk (Walton et al. 2013). Despite the presence of a warm absorber, Mrk 509 can still be considered a "bare" AGN. The intrinsic absorption is low enough that it does not complicate determination of the reflection continuum (Walton et al. 2013).

Most of the previous analyses of Mrk 509 mentioned above have predominantly focused on understanding the physical details of the warm absorber, the soft excess and the high-velocity outflows. Our emphasis is upon the detection or not of *relativistic reflection* features, namely the Fe K complex and the Compton hump, which are likely to originate due to the reprocessing of hard X-rays in the inner-most regions of the accretion disk. To date, observations of the hard X-ray component in which these signatures are most evident are quite limited, and the physical picture is accordingly subject to large and fundamental uncertainties (e.g., Petrucci et al. 2013; Ponti et al. 2013; Kaastra et al. 2014).

Table 1. Observational Data Log for Mrk 509

Telescope	Instrument	ObsId	Date	Exp (ks)	Counts (10^5)
NuSTAR	FPMA/B	60101043002	2015-04-29	166	3.2
NuSTAR	FPMA/B	60101043004	2015-06-02	37	0.6
Suzaku	XIS 0/3	410017010	2015-05-01	47	2.1

The *Nuclear Spectroscopic Telescope Array* (*NuSTAR*, Harrison et al. 2013) low background, high sensitivity and ∼ 3–79 keV bandwidth (which captures the key reflection features), together with the development of advanced relativistic reflection models such as `relxill` (Dauser et al. 2013; García et al. 2013, 2014), have revolutionized studies of X-ray reflection spectroscopy (e.g., Risaliti et al. 2013; Walton et al. 2014; Keck et al. 2014; Kara et al. 2017; Porquet et al. 2018). In this paper, we present analysis of the first *NuSTAR* and the last *Suzaku* observations of the bright AGN Mrk 509. Implementing a variety of X-ray spectral models, we investigate the origin of the soft excess and the possibility for relativistic ionized reflection in this source. Based on these fits, we present a theoretical discussion on the physical implications of two competing models to explain the soft excess: the warm corona and the relativistic reflection.

2. OBSERVATIONAL DATA

The first *NuSTAR* observations of Mrk 509 were taken during Cycle 1 of the Guest Observer Program on 2015-April-29, with a total requested exposure time of 200 ks. A simultaneous *Suzaku* observation was performed with a 50 ks exposure in order to provide low energy coverage. The *NuSTAR* exposure was interrupted after ∼165 ks due to a Target of Opportunity trigger. The remaining ∼35 ks were taken roughly a month later on 2015-June-02. A log with details of the observational data analyzed in this paper is shown in Table 1.

2.1. *NuSTAR Extraction*

The *NuSTAR* data are split over two ObsId, 60101043002 and 60101043004, separated by roughly a month. We reduced these data following standard procedures using the *NuSTAR* Data Analysis Software (NUSTARDAS, v1.6.0) and instrumental calibration files from caldb v20160824. We first cleaned the unfiltered event files with NUPIPELINE. We used the standard depth correction, which significantly reduces the internal high-energy background, and also removed passages through the South Atlantic Anomaly, again using standard filtering parameters. Source and background spectra/lightcurves and instrumental responses were then produced for both focal plane modules FPMA and FPMB using

NUPRODUCTS. Source products were extracted from circular regions of radius 120″, and background was estimated from regions of blank sky on the same detector as Mrk 509. In order to maximize the signal-to-noise (S/N), in addition to the standard 'science' (mode 1) data, we also extracted the 'spacecraft science' (mode 6) data following Walton et al. (2016). In this case, the mode 6 data provide ∼10% of the total ∼220 ks good *NuSTAR* exposure.

2.2. *Suzaku Extraction*

The *Suzaku* data were reduced starting from the unfiltered event files and then screened applying the standard selection criteria described in the *Suzaku* ABC guide[1]. The source spectra were extracted from circular regions of 2.5′ radius centered on the source, whereas background spectra were extracted from a region of the same size offset from the main target and avoiding the calibration sources. We generated the redistribution matrix file (RMF) and the ancillary response file (ARF) of the X-ray Imaging Spectrometer (XIS) with the `xisrmfgen` and `xissimarfgen` ftools, respectively. We selected the XIS data in both the 3×3 and 5×5 modes. The spectra were inspected for possible pile-up contamination and this possibility was excluded. The spectra of the front-illuminated XIS instruments (XIS 0 and XIS 3) were merged after checking that their fluxes were consistent. The data from the back-illuminated XIS instrument, XIS 1, is not used due to its much lower sensitivity in the Fe K band and cross-calibration uncertainties with the front-illuminated XIS 0 and XIS 3.

2.3. *Light Curves and Time-Averaged Spectra*

The lightcurves for the two *NuSTAR* and the *Suzaku* exposures are shown in Figure 1. The data were binned in 2 ks intervals. The *Suzaku* exposure is simultaneous with the first and longer *NuSTAR* exposure. The lightcurves show a very similar level of variability, which in both cases is very weak (∼ 6%). This value corresponds to the normalized excess variance (Vaughan et al. 2003) that suppresses a possible rms-flux correla-

---

[1] http://heasarc.gsfc.nasa.gov/docs/suzaku/analysis/abc/
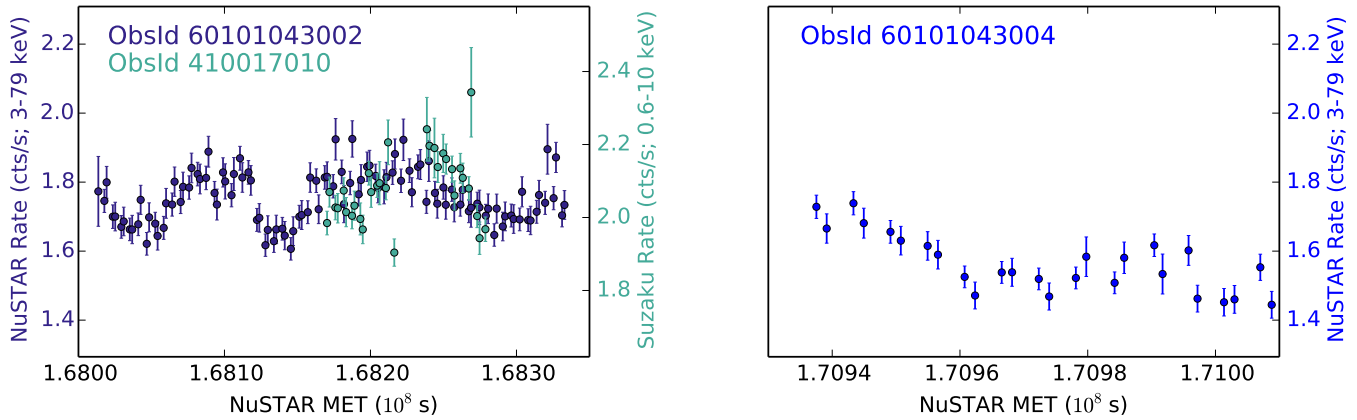
Figure 1. Light curves for the *NuSTAR* FPMA and *Suzaku* XIS exposures of Mrk 509 binned in 2 ks intervals. The left panel shows the first ∼165 ks *NuSTAR* exposure (ObsId 60101043002), together with the ∼50 ks *Suzaku* exposure (ObsId 410017010), while the right panel shows the shorter ∼65 ks *NuSTAR* observation (ObsId 60101043004). The source shows a very stable count rate through the full range, with no obvious flares or dips.

tion usually found for un-normalized rms measures. The right panel of Figure 1 contains the lightcurve for the shorter *NuSTAR* exposure taken roughly a month later. It shows a similar count rate with no significant variability; neither flares nor strong dips are detected. Spectra extracted from the two *NuSTAR* exposures imply consistency after visual inspection. We therefore combined these into a single spectrum taking advantage of the full ∼220 ks exposure.

The final extracted total count spectra for *NuSTAR*'s FPMA and FPMB, and *Suzaku*'s XIS instruments are shown in Figure 2. The shaded region depicts the corresponding backgrounds, which are well below the source counts up to ∼50 keV. We include *Suzaku* data in the 1–8 keV range, excluding the 1.7–2.5 keV range due to calibration uncertainties. We ignore data below 1 keV due to concerns over the quality of the calibration given molecular contamination of the XIS detectors; contamination reduces the effective area differently on each detector, and as a function of off-axis angle (Koyama et al. 2007; Kettula et al. 2013), and it is expected to worsen over time (Madsen et al. 2017). *NuSTAR* data is included in the 3–79 keV range. The spectra were rebinned in order to oversample the instrument's resolution by a factor of 3, and to ensure a minimum signal-to-noise of 6 per bin.

3. SPECTRAL ANALYSIS

We simultaneously fit the two *NuSTAR* FPMA and FPMB spectra extracted from the full ∼220 ks exposure together with the ∼ 50 ks *Suzaku* spectrum. The fitting and statistical analysis presented here was carried out using the XSPEC package v-12.9.0d (Arnaud 1996). A cross normalization constant is included to account for differences in the flux calibration among all three instru-

ments (i.e., FPMA, FPMB, and XIS). The fitted values are consistent with those previously reported by Madsen et al. (2015). All model parameter uncertainties are quoted to 90% confidence level.

Figure 2 (right) shows the data-to-model ratio of these observations when fitted with a simple absorbed power-law model (i.e., TBabs*pow). The TBabs component is used to describe the Galactic absorption (see Section 3.1). The typical signatures of X-ray reflection off optically thick material are evident in the spectrum: the fluorescent iron emission near 6.4 keV, the iron K-edge near 7 keV, and the Compton hump peaking at ∼25 keV. Both instruments satisfactorily agree in the shape and intensity of the iron emission. In absence of relativistic effects, these features are well described by the reprocessing of the X-rays in a relatively cold and neutral material, located far away from the central region, possibly at the broad line region (e.g., Costantini et al. 2016; Nardini et al. 2016), or even at the torus (e.g., Yaqoob et al. 2007; Murphy & Yaqoob 2009; Marinucci et al. 2018).

The nature of the soft excess in *Suzaku*'s bandpass, however, is not yet very well established. As we shall show next, the particular choice of the components used to model the soft excess has an important effect in modeling of the reflected spectrum, and in fact leads to different interpretations for this system. We will then present fits with two different scenarios, and later discuss the physical interpretation and implications for each one.

3.1. *Approach 1: Fitting the Soft Excess with a Warm Corona*

In their analysis of the *XMM-Newton* and *INTE-GRAL* campaign, Petrucci et al. (2013) proposed that the clearly observed soft excess in Mrk 509 is due to the
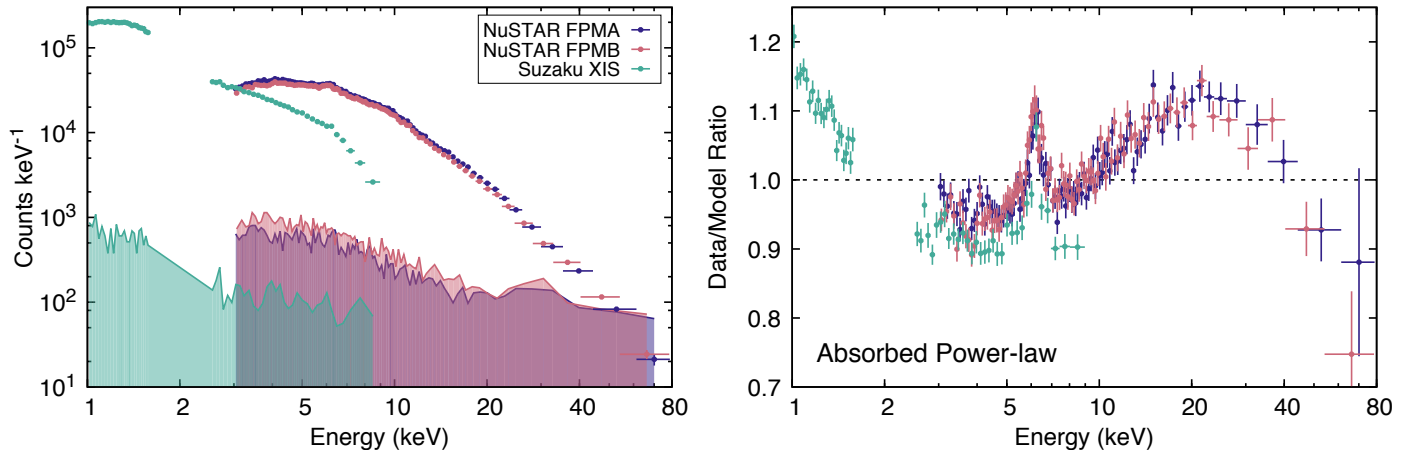
Figure 2. Left: Count spectra from the 50 ks *Suzaku* XIS (green) and the 220 ks *NuSTAR* FPMA/B (blue/red) exposures. The shaded regions show the level of background for each of the instruments. Right: Ratio of the data to an absorbed power-law model, showing the soft excess at $\sim 1\,\text{keV}$, the Fe K emission at $\sim 6.4\,\text{keV}$, and the Compton hump at $\sim 20-30\,\text{keV}$.

presence of a warm corona, which they reproduced using a Comptonization model. This corona can then be visualized as a warm ($kT_\text{e} \sim 0.5-1\,\text{keV}$) but optically thick ($\tau \sim 10-20$) atmosphere sitting on top of the accretion disk. This extended, slab-like corona is much colder than the centrally located and possibly spherical corona responsible for the power-law continuum emission that extends to high energies. The emission of the hot corona was fitted with a second Comptonization model, with a higher coronal temperature ($kT_\text{e} \sim 100\,\text{keV}$) and lower optical depth ($\tau \sim 0.5$).

We adopted the prescription of Petrucci et al. (2013) to fit the soft excess. For this, we implemented two Comptonization components using the `nthComp` model (Zdziarski et al. 1996; Życki et al. 1999) with the required parameters to reproduce the power-law continuum (hot corona) and the soft excess (warm corona). The hot corona component is characterized by a slope of $\Gamma \sim 1.84$ and a relatively low electron temperature of $kT_\text{e} \sim 30\,\text{keV}$. The temperature of the seed photons for this component cannot be constrained and it is thus fixed to a relatively low value ($kT_\text{BB} = 100\,\text{eV}$). The warm corona component is characterized by a very soft continuum fixed at $\Gamma = 2.5$ and a much colder electron temperature $kT_\text{e} \sim 0.4-0.5\,\text{keV}$, as well as a much lower temperature for the seed photons, fixed at $kT_\text{BB} = 3\,\text{eV}$. The parameters held fixed in these two components cannot be constrained with the current dataset, likely due to the lack of data below 1 keV. Their values were chosen following the best-fit results of Petrucci et al. (2013). The intrinsic galactic absorption in this system is modeled using the `TBabs` model with the corresponding abundances as set by Wilms et al. (2000). This model automatically implements the Verner et al.

(1996) photoelectric cross sections. We freeze the column density to $N_\text{H} = 4.25 \times 10^{20}\,\text{cm}^{-2}$ (Kalberla et al. 2005), and the source redshift to $z = 0.035$.
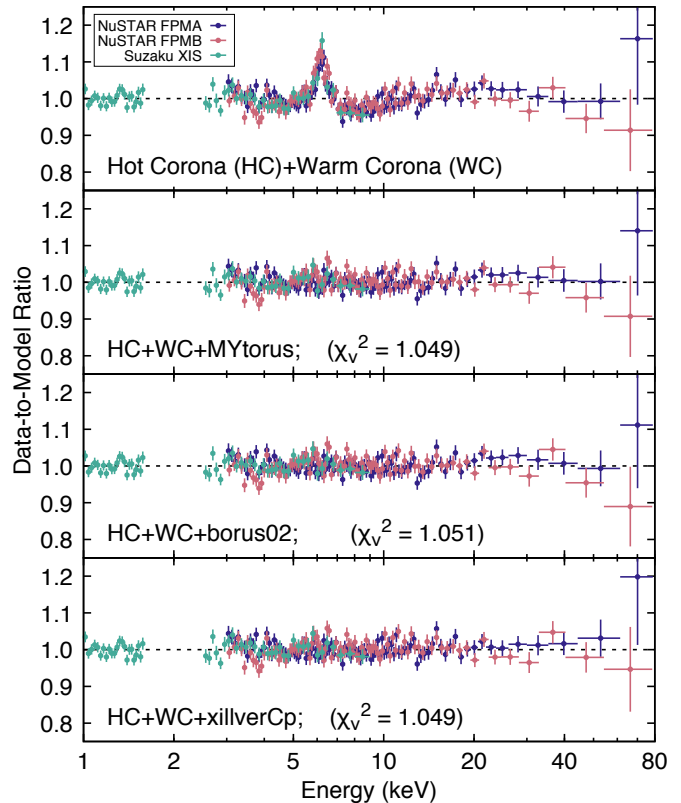
A data-to-model ratio plot of the fit using these models for the continuum is shown in the top panel of Figure 3. These two Comptonization components, which are independent from one another, provide a good fit to both the continuum and the soft excess, and the only obvious residuals are those from the Fe K fluorescence emission due to X-ray reflection.

The residuals that remain after fitting the continuum can be well fitted with a distant reflection model component, in which the gas is assumed either to be completely neutral or at a very low ionization stage, and no relativistic effects are included. We have tested this idea by implementing three different (non-relativistic) reflection models, namely, `MYtorus`, `borus02`, and `xillverCp`, which we describe below. The residuals of these fits are shown in the last three panels of Figure 3, and the best-fit values summarized in Table 2.

Model 1.1: The `MYtorus` reflection model (Murphy & Yaqoob 2009) calculates the attenuation in the line-of-sight of X-rays produced by a central source, together with the scattered continuum, and the fluorescence emission from neutral iron and nickel, assuming a toroidal geometry. In this model, the X-ray source emits a power-law continuum with no cutoff at high energies. All elemental abundances are at their Solar values. In our fit, all the parameters of the transmitted and scattered components are tied to each other. The photon index is linked to the one from the hot-corona component. The inclination is fixed to 60°, as it has no appreciable effect on the fit. Thus, the column density and normalization are the only free parameters.

Model 1.2: The `borus02` model (Baloković et al. 2018), is similar to MYtorus in nature, but is more flexible as it provides additional tunable spectral parameters such as the high-energy cutoff in the intrinsic continuum, the torus covering factor, and the relative abundance of iron. The approximately toroidal geometry assumed for the model employed here[2] is the same as in the popular model by Brightman & Nandra (2011), but the model is updated, expanded, and corrected for known issues as described in Liu & Li (2015) and Baloković et al. (2018). Like MYtorus, `borus02` allows us to model the average column density of the torus separately from the line-of-sight column density through the spectral shape of the reflection from material outside of our line of sight. As before, the inclination is degenerate in our fits, which allows us to fix it at $60°$. Again, the photon index is linked to the one describing the Comptonized emission of the hot corona. Furthermore, the covering fraction was fixed to 50%, and and the iron abundance is set to its Solar value. Finally, the simple relation $E_{cut} \sim (2-3)kT_e$ is used to link the cutoff at high energies with the electron temperature of the hot corona (e.g.; Petrucci et al. 2001; García et al. 2015). While this is a crude approximation that depends on the combination of temperature, optical depth, and geometry, we found that it is adequate for this model fit. First, the value of E_{cut} is unconstrained when set free to vary in the `borus02` model, while all the other model parameters remain unchanged. Furthermore, replacing the Comptonization continuum by a simple cutoff power-law model provides an identical fit with $E_{cut} = 95 - 175\,\mathrm{keV}$ (90% confidence), consistent with $E_{cut} \sim 3kT_e$. Thus, we use this relation to link the cutoff in the reflection model with the temperature of the hot corona. As in the case of Model 1.1, the only free parameters are the column density and the normalization.

Model 1.3: We reproduced the observed residuals with our ionized reflection model `xillverCp`. This particular flavor of the model computes the reflected spectrum using an illumination continuum produced by the Comptonization model `nthComp`. `nthComp` is a more physically consistent treatment than the standard and commonly used power-law continuum with an exponential cutoff. While `xillverCp` has a more accurate treatment of the reflection by self-consistently solving the ionization balance and radiative transfer, the geometrical considerations are much more simplistic than in MYtorus or `borus02`. In `xillverCp` a single zone, plane-parallel slab is assumed. Despite this approximation, this model also

---

[2] We used table model `borus02_afe1p00_v161220.fits` available at www.astro.caltech.edu/~mislavb/download.
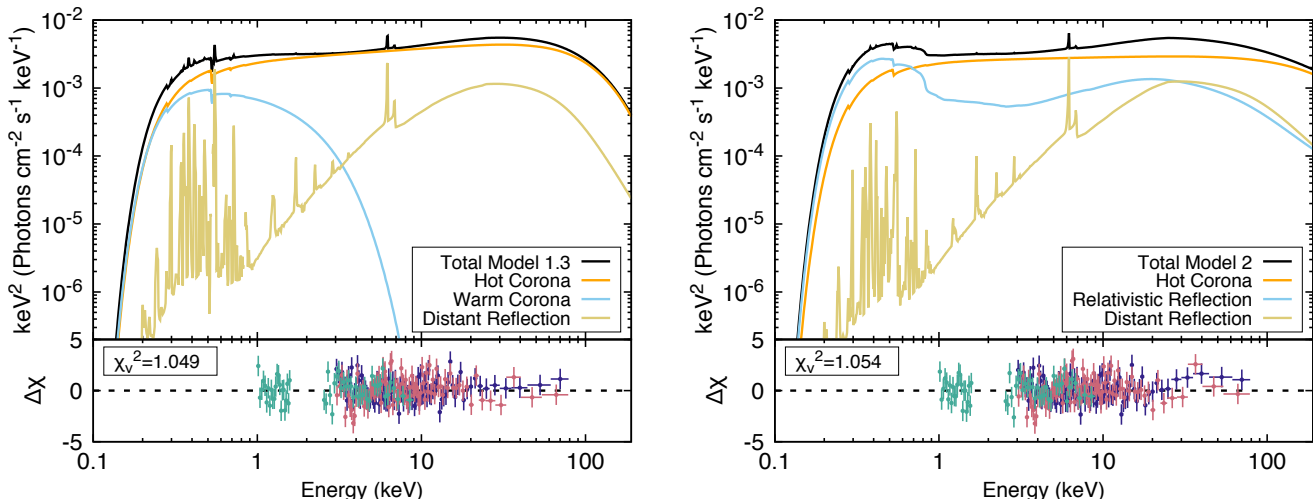

Figure 3. Data-to-model ratios for the fits with the warm corona and different models for the distant reflection.

provides a satisfactory fit to the data (Figure 3, bottom panel). As before, the slope of the illumination is fixed to that in the hot-corona model. Moreover, we fixed the ionization parameter, defined as the ratio of the ionizing flux to the gas density ($\xi = 4\pi F_x/n_e$) to its minimum value in the model order to mimic reflection off neutral gas ($\log \xi/\mathrm{erg\,cm\,s^{-1}} = 0$). We assumed Solar abundance of iron. In this case, the inclination has a small but noticeable effect in the fit, with the best-fit value pegged at its maximum ($i = 89°$). Fixing the inclination to a more reasonable value (e.g., $i = 60°$) worsens the fit significantly ($\Delta\chi^2 \sim 60$), due to strong residuals at high energies and near the Fe K band. While this could be taken as the possible presence of a broad Fe line component, its statistical significance is low. Moreover, given the simplicity of the `xillverCp` model in its geometrical considerations, we do not interpret the derived inclination as a meaningful estimate. In addition to the inclination, the normalization is the only other free parameter in this fit.

From a statistical point of view, these three models are indistinguishable. Only very small differences in the goodness of the fit are apparent in the bottom of Table 2. From these, the fit with the `borus02` model

Figure 4. Model components (top panels) and residuals (bottom panels) for the best fits using the warm corona approach (Model 1.3, left) and the relativistic reflection approach (Model 2, right) to describe the soft excess observed in Mrk 509.

(Model 1.2) is slightly worse, but with a marginal increase in χ^2 of ~ 4 when compared to the other two. From the ratio plots shown in Figure 3, it appears that these three models perform equally well in describing the data. Despite some small differences, these three fits share the same relevant aspects. First, no inner-disk (relativistic) reflection is required in any of the fits, as no significant residuals remain in the Fe K region. Second, the electron temperature of the hot corona is relatively low ($kT_e^{HC} \sim 30\,\mathrm{keV}$), which suggests a low energy cutoff in the continuum. Finally, the electron temperature of the warm corona is similar in all the fits at $kT_e^{WC} \sim 0.4-0.5\,\mathrm{keV}$, which is consistent with values previously derived by Petrucci et al. (2013).

3.2. *Approach 2: Fitting the Soft Excess With Relativistic Reflection*

Another approach that has been proposed in the past to explain the soft excess in AGN is relativistic reflection (e.g., Crummy et al. 2006; Fabian et al. 2009; Nardini et al. 2012; Walton et al. 2013). As the X-rays from the central source illuminate the inner regions of the accretion disk, the reflected or reprocessed radiation displays a spectrum rich in fluorescence lines and other atomic features. This spectrum is particularly populated with emission lines in the low energy range ($\lesssim 1\,\mathrm{keV}$), where most of the K-shell transitions from low-Z elements occur. As the reprocessing is produced near the supermassive black hole, relativistic effects will blur and skew all the atomic features, effectively smoothing the entire reflected spectrum. As a result, this component can in fact produce enough flux at low energies to explain the observed soft excess. Furthermore, we have recently shown that this effect is further enhanced if the density of the

reflecting material lies above the typically assumed value of $n_e = 10^{15}\,\mathrm{cm}^{-3}$, due to the extra heating produced by the increased free-free emission (García et al. 2016).

In order to test this approach, we replaced the warm-corona component with a relativistic-reflection component. For this, we implemented our model `relxillD`, which describes both the incident Comptonized continuum and the reflection spectra calculated with our code `xillver` (García & Kallman 2010; García et al. 2013) in the case of a high-density gas (`xillverD`, García et al. 2016), taking into account all the relativistic effects (Dauser et al. 2013; García et al. 2014). While the `relxillD` model has the advantage of providing the gas density as a free parameter, one limitation is that the illumination continuum assumed is a power-law spectrum with an e-folded cutoff fixed at $300\,\mathrm{keV}$ (instead of the Comptonization continuum used in `xillverCp`). However, freeing up the cutoff energy will only introduce a significant effect in the fit if the curvature imprinted in the power-law continuum falls within the covered bandpass and it can be detected given the instrument's signal-to-noise.

In this fit, from here on Model 2, the distant (non-relativistic) reflection is still modeled with `xillverCp`, as in Model 1.3. For the relativistic reflection, we use the specific flavor of `relxillD`, namely `relxilllpD`, in which a lamppost geometry is assumed for the hot corona (Dauser et al. 2013, 2016) that is self-consistently linked with the reflected continuum. The slopes of both the distant and inner-disk reflection components are tied to that in the hot corona, as well as the electron temperature in `xillverCp`. The inclination of the system is tied among the two reflection components. Unlike the previous fits with Models 1.1–1.3, in this case the

Table 2. Best-fit parameters and fit statistics for the three models featuring a warm corona prescription.

Description	Component	Parameter	Model 1.1	Model 1.2	Model 1.3
Galactic Absorption	TBabs	$N_{\rm H}$ (10^{20} cm^{-2})	4.25	4.25	4.25
Hot Corona	nthComp	$kT_{\rm BB}$ (eV)	100	100	100
Redshift	nthComp	z	0.035	0.035	0.035
Warm Corona	nthComp	$kT_{\rm BB}$ (eV)	3	3	3
	nthComp	Γ	2.5	2.5	2.5
Hot Corona	nthComp	Γ	1.84 ± 0.01	1.83 ± 0.01	1.84 ± 0.01
	nthComp	$kT_{\rm e}^{\rm HC}$ (keV)	26^{+6}_{-4}	29^{+6}_{-4}	29^{+6}_{-4}
	nthComp	$N_{\rm HC}$ (10^{-2})	1.33 ± 0.02	1.32 ± 0.02	1.29 ± 0.02
Warm Corona	nthComp	$kT_{\rm e}^{\rm WC}$ (keV)	0.39 ± 0.07	0.40 ± 0.07	$0.50^{+0.05}_{-0.08}$
	nthComp	$N_{\rm WC}$ (10^{-2})	0.34 ± 0.07	0.35 ± 0.06	0.37 ± 0.07
Neutral Reflection	MYtorus	$N_{\rm H}$ (10^{24} cm^{-2})	1.06 ± 0.14	$\cdots$	$\cdots$
	MYtorus	$N_{\rm MY}$[b]	1.25 ± 0.12	$\cdots$	$\cdots$
Neutral Reflection	Borus02	$N_{\rm H}$ (10^{24} cm^{-2})	$\cdots$	1.17 ± 0.20	$\cdots$
	Borus02	$N_{\rm B}$[b]	$\cdots$	0.93 ± 0.08	$\cdots$
Neutral Reflection	xillverCp	i (deg)	$\cdots$	$\cdots$	89[a]
	xillverCp	$N_{\rm Xi}$ (10^{-2})[b]	$\cdots$	$\cdots$	$0.25^{+0.02}_{-0.01}$
Cross-normalization	*NuSTAR* FPMB	$C_{\rm FPMB}$	1.026 ± 0.005	1.026 ± 0.005	1.026 ± 0.005
	Suzaku XIS	$C_{\rm XIS}$	0.95 ± 0.04	0.95 ± 0.03	0.95 ± 0.03
		χ^2	1799.5	1804.0	1800.4
		ν	1716	1716	1716
		χ^2_ν	1.049	1.051	1.049

[a] Parameter pegged at its maximum value.

[b] Model normalizations in 10^{20} photons cm^{-2} s^{-1}.

Note—Model 1.1: `TBabs*(nthComp+nthComp+MYtorus)`, Model 1.2: `TBabs*(nthComp+nthComp+borus02)`, and Model 1.3: `TBabs*(nthComp+nthComp+xillverCp)`. The parameters listed in the first block were assumed fixed at the same value in all the models.

electron temperature of the hot corona is loosely constrained. Fixing $kT_{\rm e} = 30$ keV (similar to the value found with the fits in Section 3.1), results in a significantly worse fit (with χ^2 increasing by ~ 40), and obvious residuals in excess at high energies. This indicates that this particular fit prefers a cutoff a much larger energies. Adopting once again the simple approximation $E_{\rm e} = 3kT_{\rm e}$, we fixed the electron temperature of the hot corona at 100 keV (i.e., one third of the cutoff energy of 300 keV in the `relxilllpD` component). The best-fit parameters are summarized in Table 3.

In terms of fit statistics, the relativistic reflection prescription reproduces the data similarly well as the warm corona prescription from Models 1. The fit with Model 2 is marginally worse, with an increase of $\Delta\chi^2 \sim 6-10$, despite using three more free parameters. It is, however, unclear if any of these fits is preferred on statistical grounds. The model components and residuals of the fits with the two scenarios (Models 1.3 and 2) are compared in Figure 4. The two models are almost identical in the band covered by the data, with the largest differences occurring around $30-60$ keV for Model 2. These residuals are possibly due to the fact that the reflection model used here was calculated using an e-folded power-law illumination spectrum with a high-energy cutoff fixed at 300 keV, rather than a proper Comptonization continuum. On the other hand, we also note that Model 2 allows for a softer continuum ($\Gamma = 1.96$) than Model 1.3 ($\Gamma = 1.84$), which can also affect the way the model fits the rollover at high energies.

Despite its statistical match, the relativistic reflection component (`relxilllpD`) requires extreme parameters, i.e., low coronal height ($h = 1.53^{+0.01}_{-0.25} R_{\rm Hor}$), and close to maximum spin ($a_* > 0.993$), together with a large gas density ($\log n_{\rm e}/{\rm cm}^{-3} > 18.2$). This configuration results in a soft and featureless spectrum, with a strong broad emission at low energies, which is required to fit the soft excess.

Table 3. Best-fit parameters and fit statistic for the model featuring relativistic reflection.

Description	Component	Parameter	Model 2
Galactic Absorption	`TBabs`	N_{H} (10^{20} cm^{-2})	4.25^{a}
Hot Corona	`nthComp`	kT_{BB} (eV)	100^{a}
	`nthComp`	z	0.035^{a}
	`nthComp`	Γ	$1.96^{+0.01}_{-0.03}$
	`nthComp`	$kT_{\mathrm{e}}^{\mathrm{HC}}$ (keV)	100^{a}
	`nthComp`	N_{HC} (10^{-2})	$1.30^{+0.01}_{-0.03}$
Relativistic Reflection	`relxilllpD`	h (R_{Hor})	$1.53^{+0.01}_{-0.25}$
	`relxilllpD`	a_* (cJ/GM^2)	> 0.993
	`relxilllpD`	i (deg)	$69.7^{+2.8}_{-1.7}$
	`relxilllpD`	$\log \xi$ (erg cm s^{-1})	$2.31^{+0.39}_{-0.15}$
	`relxilllpD`	A_{Fe} (Solar)	< 0.82
	`relxilllpD`	$\log n_{\mathrm{e}}$ (cm^{-3})	> 18.2
	`relxilllpD`	N_{r} (10^{-2})$^{\mathrm{b}}$	$2.23^{+9.95}_{-0.44}$
Distant Reflection	`xillverCp`	N_{x} (10^{-4})$^{\mathrm{b}}$	$2.02^{+0.34}_{-0.13}$
Cross-normalization	*NuSTAR* FPMB	C_{FPMB}	1.026 ± 0.005
	Suzaku XIS	C_{XIS}	0.95 ± 0.02
	Flux (erg cm^{-2} s^{-1})	2–10 keV	4.6×10^{-11}
		20–40 keV	3×10^{-11}
	χ^2		1806.1
	ν		1713
	χ^2_{ν}		1.054

[a]Parameter fixed to the quoted value.

[b]Model normalizations in 10^{20} photons cm^{-2} s^{-1}.

NOTE—Model 2: `TBabs*(nthComp+relxillD+xillverCp)`.

4. DISCUSSION

In the previous section we presented several model fits to the observational data of Mrk 509. These models are based on two different scenarios to explain the origin of the soft excess in the spectrum: the warm corona and the relativistic reflection picture. In either case, strong signatures of reflection are observed (i.e., Fe K emission and K edge, plus a Compton hump). This signal is consistent with low-ionization reflection from a structure located at a farther distance such that no relativistic effects are observed. Models for Compton-thick AGN (`MYtorus` and `borus02`; Models 1.1 and 1.2), and nearly-neutral reflection from a single plane-parallel slab (`xillverCp`; Model 1.3) all provide equally good fits to the data. This implies that the geometrical considerations for the distribution of gas in the line-of-sight are relatively unimportant. Moreover, we notice that no other components are required to fit the Fe K emission, while Ponti et al. (2013) reported both a narrow ($\sigma = 0.027$ keV), plus a resolved ($\sigma = 0.22$ keV) Gaussian feature for the Fe K line in their analysis of previous *Chandra* grating data. However, these two components were unresolved in their *XMM-Newton* and *Suzaku* data, and likewise are expected to be unresolved in our *XMM-Newton* and *NuSTAR* data. This is possibly the reason why Models 1.1–1.3 are able to reproduce the spectral features without any additional components. Weak ionized emission features were also reported by Ponti et al. (2013), which could be attributed to Fe XXV-XXVI. We do not find evidence for these additional components, possibly due to the lower signal-to-noise of our data.

For the sake of comparison, we will now focus on the fits performed with Models 1.3 (warm corona) and Model 2 (relativistic reflection at high densities), and discuss the physical implications of each scenario.

4.1. *Implications of the Warm Corona Model*

In the warm corona model, the soft emission observed in excess of the hard power-law continuum originates in

Comptonization of thermal disk photons into a warm ($T \sim 0.5 - 1\,\mathrm{keV}$ or $\sim 0.6 - 1.2 \times 10^7\,\mathrm{K}$) and optically thick ($\tau_\mathrm{T} \sim 10 - 20$) corona (Walter & Fink 1993; Magdziarz et al. 1998; Done et al. 2012). This warm corona has been described as a slab sitting on top of a passive accretion disk covering roughly 10–$20\,R_\mathrm{g}$ of the inner region (e.g., Petrucci et al. 2013). One argument that favors this scenario is the observed correlation between the optical-UV and the soft X-ray emission (Mehdipour et al. 2011). As shown in our fits to Models 1.1-1.3, the warm corona model provides a satisfactory description of the data in combination with a distant reflection component, without the requirement of relativistic reflection.

In this case, the temperature of the hot corona (the one responsible for the hard power-law continuum) is found to be relatively low ($kT_\mathrm{e} \sim 25 - 35\,\mathrm{keV}$ or $\sim 3 - 4 \times 10^8\,\mathrm{K}$). While low coronal temperatures were not common in earlier studies of AGN (e.g., Marinucci et al. 2016), several recent *NuSTAR* measurements have reported relatively cold coronae, namely $\sim 50\,\mathrm{keV}$ (IC 4329A, Brenneman et al. 2014), $\sim 25\,\mathrm{keV}$ (MCG$-$05-23-016, Baloković et al. 2015), $\sim 40\,\mathrm{keV}$ (NGC 5548, Ursini et al. 2015), $\sim 12\,\mathrm{keV}$ (GRS 1734$-$292, Tortosa et al. 2017), $\sim 35\,\mathrm{keV}$ (IRAS 05189$-$2524, Xu et al. 2017), and $\sim 15\,\mathrm{keV}$ (Ark 564, Kara et al. 2017). Moreover, Ricci et al. (2017) have also reported a handful of sources with low cutoff energies fitting e-folded power-law models to sources from the *Swift*/BAT sample, and found that those sources appear to be the ones with the highest Eddington ratios. Meanwhile, Tortosa et al. (2018) have reported more reliable coronal temperatures for a sample of AGN by implementing thermal Comptonization models, in which most of the sources are found to have coronal temperatures below $\sim 60\,\mathrm{keV}$.

While the warm-corona model has been successfully used in several other sources (see Petrucci et al. 2018, and references therein), its physical origin and implications have yet to be fully explained. Czerny et al. (2003) argued that a warm Comptonizing skin on top the accretion disk under radiation pressure instabilities could explain the observed X-ray spectra from quasars and narrow line Seyfert AGN. Różańska et al. (2015) investigated the properties of such a corona by solving the radiative transfer for a grey atmosphere. More recently, Petrucci et al. (2018) presented a theoretical discussion to explain the warm corona based on simple photon conservation arguments, concluding that most of the energy dissipation takes place in the warm corona rather than in the accretion disk. Meanwhile, Kaufman et al. (2018) proposed that bulk Comptonization from turbulence due to magneto-rotational instabilities can explain the warm corona. These authors argue, however, that this picture is only applicable to systems with high accretion rate, possibly of the order or larger than the Eddington limit. Crucially, all these theoretical studies share the same fundamental limitation: they neglect the effects of atomic photoelectric absorption, which is likely to be a dominant process in optically-thick atmospheres.

It is interesting to describe the basic properties of the warm corona based on the average quantities obtained from fits to observational data (e.g., $\tau_\mathrm{T} \sim 10$ and $kT_\mathrm{e} \sim 0.5\,\mathrm{keV}$, Petrucci et al. 2018). The vertical extension of this corona can be estimated as

$$z = \tau_\mathrm{T}/(\sigma_\mathrm{T} n_\mathrm{e}), \qquad (1)$$

where $\sigma_T = 6.65 \times 10^{-25}\,\mathrm{cm}^2$ is the Thomson cross section and n_e is the electron density. Therefore $z \sim 1.5 \times 10^{24} \tau_\mathrm{T} n_\mathrm{e}^{-1}\,\mathrm{cm}$, or in units of the gravitational radius $R_g = GM/c^2 \approx 1.5 \times 10^{13}(M_8/M_\odot)\,\mathrm{cm}$,

$$z/R_g \sim 10^{11}(M_8/M_\odot)(\tau_\mathrm{T}/n_\mathrm{e}), \qquad (2)$$

where G is the gravitational constant, c is the speed of light, and $M_8 = 10^8 M_\odot$. In the case of Mrk 509, $M_8/M_\odot \sim 1$ (Peterson et al. 2004), and thus the density must be of the order of $n_\mathrm{e} \sim 10^{12}\,\mathrm{cm}^{-3}$ or higher for the warm corona to have a reasonable ($z \sim R_g$) geometrical thickness. Moreover, for sources with $M \sim 10^5$–$10^6 M_\odot$, this estimate implies densities for the warm corona of the order of the typical values used for the accretion disk atmosphere in X-ray reflection calculations (e.g., $n_\mathrm{e} \sim 10^{15}\,\mathrm{cm}^{-3}$; Ross & Fabian 2005; García & Kallman 2010).

One requirement for the warm corona scenario is to ensure that electron scattering is the dominant source of opacity. However, Krolik & Kallman (1984) showed that for an optically-thin gas under coronal ionization equilibrium (CIE), the photoelectric opacity dominates the soft band for $T \sim 10^6\,\mathrm{K}$, and even at $T \sim 10^7\,\mathrm{K}$ it is comparable to the Thomson opacity at $\sim 1\,\mathrm{keV}$ (see their Fig. 1). We have tested this argument by computing simulations for an optically-thick plasma under CIE using the latest version of the XSTAR code (Kallman & Bautista 2001), with the appropriate parameters that describe a warm corona: $n_\mathrm{e} = 10^{12}\,\mathrm{cm}^{-3}$, $\tau_\mathrm{T} = 6.65$ (corresponding to the maximum column allowed by the model, $N_\mathrm{H} = 10^{25}\,\mathrm{cm}^{-2}$), $L_\mathrm{x} = 10^{46}\,\mathrm{erg\,s}^{-1}$ (which is in fact larger than the value typically measured for this source), and cosmic abundances. The incident spectrum is assumed to be a blackbody at the given gas temperature. Figure 5 (left) shows the resulting photoelectric opacity as function of energy for different gas
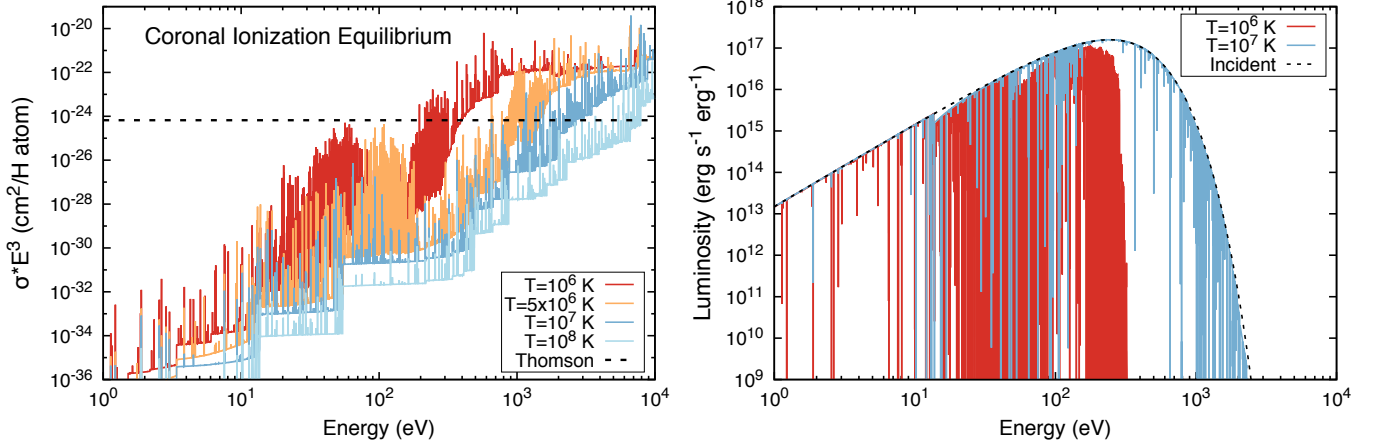
Figure 5. Calculations for a gas under coronal ionization equilibrium for different temperatures (as indicated), and the parameters that describe a warm corona: $n_e = 10^{12}\,\text{cm}^{-3}$, $\tau_T = 6.65$, and $L = 10^{46}\,\text{erg s}^{-1}$. The left panel shows the photoelectric opacity as a function of energy, compared to the Thomson electron opacity. The right panel shows the resulting transmitted spectra. For clarity, only two cases are displayed, those for the lowest and highest temperatures derived from fitting the warm corona model to observational data. The incident blackbody spectrum for the $T = 10^7\,\text{K}$ is also shown.

temperatures, in comparison with the Thomson opacity for electron scattering σ_T. This demonstrates that even in the optically-thick case, photoelectric opacity dominates over a wide range of energies, particularly around or above 1 keV, for the range of temperatures required by the warm corona, i.e., $kT \sim 0.1 - 1\,\text{keV}$ ($T \sim 10^6 - 10^7\,\text{K}$). The right panel in Figure 5 shows the transmitted spectra for these two CEI calculations. At $T = 10^6\,\text{K}$ the original disk blackbody emission is heavily absorbed and modified, with strong photo-absorption at almost all energies and with no emission above $\sim 300\,\text{eV}$. The situation is better at $T = 10^7\,\text{K}$, although strong absorption is still present, particularly around 0.1 keV and 1 keV. We found in general that for electron scattering to be a dominant source of opacity, temperatures well above $10^7\,\text{K}$ are required.

Another possibility is to instead invoke a gas under photoionization equilibrium, since a radiation field strong enough can be responsible for stripping most of the ions and thus considerably reducing the total photoelectric opacity. This is in fact relevant since one expects the ionization of the warm corona to be fairly large, from simple arguments. We start by using the standard definition of the ionization parameter $\xi = L/(n_e R^2)$, where L is the luminosity and R is the distance from a generic source of radiation (e.g., the hot corona) to the warm corona. For a thin disk, $z/R =$ constant~ 0.1, and using Equation 1

$$\xi = 10^{-1} \frac{\sigma_T L}{\tau_T R} \qquad (3)$$

or

$$\xi\,[\text{erg cm s}^{-1}] \sim 10^7 (L/L_{\text{Edd}})(R/R_g)^{-1}, \qquad (4)$$

where $L_{\text{Edd}} = 1.26 \times 10^{46}(M_8/M_\odot)\,\text{erg s}^{-1}$ is the Eddington luminosity. So for $L/L_{\text{Edd}} = 0.1$ and $R = 10 R_g$, $\xi \sim 10^5\,\text{erg cm s}^{-1}$. A different estimate can be made if the ionization is assumed to be due to the thermal emission from the accretion disk. Using the definition of the ionization parameter $\xi = 4\pi F/n_e$, and the local flux from the disk

$$F_d = \frac{3\pi}{8} \frac{GM\dot{M}}{R^3} \qquad (5)$$

and $\dot{M} = L/(\eta c^2)$, we find

$$\xi = \frac{0.15\pi^2 \sigma_T G}{\tau_T \eta c^2} \frac{ML}{R^2}, \qquad (6)$$

where $\eta \approx 0.1$ is the accretion efficiency. This last equation can be rewritten as

$$\xi\,[\text{erg cm s}^{-1}] \sim 10^9 (L/L_{\text{Edd}})(R/R_g)^{-2}, \qquad (7)$$

and thus for $L/L_{\text{Edd}} = 0.1$ at $R = 10 R_g$ we get $\xi \sim 10^6\,\text{erg cm s}^{-1}$. While this expression results in a larger ionization than the estimate in Equation 4, it decreases quadratically (rather than linearly) with radius. It is also interesting that both expressions are independent of the black hole mass.

Although Equations 4 and 7 predict fairly large ionization for the warm corona, this is only true for the case of an optically-thin slab. For large optical depths ($\tau_T \simeq 1$), the ionization will quickly decrease in the deeper regions of the gas, and photoelectric absorption can be as important or more than the Thomson opacity. These results are generally in line with the seminal calculations presented by Ross et al. (1978), where they considered the photoionization of isothermal spheres at $T = 10^6 - 10^7\,\text{K}$, with $\tau_T = 6$, and $n_e = 10^{16}\,\text{cm}^{-3}$.
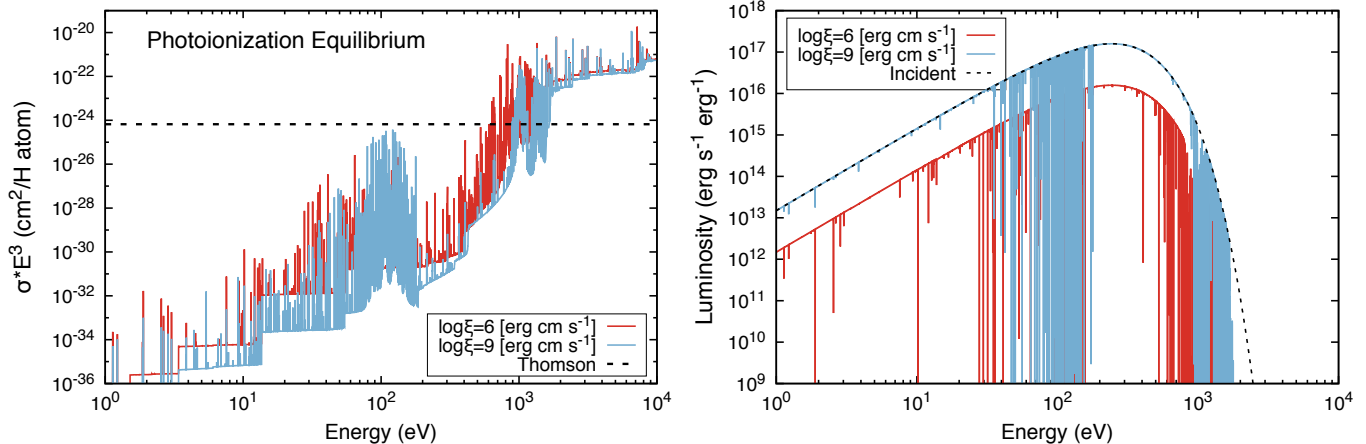
Figure 6. Calculations similar to those in Figure 5, but for the case of a gas under photoionization equilibrium, at two different ionizations: $\xi = 10^6$ and $10^9 \, \mathrm{erg\,cm\,s^{-1}}$. As before, left panel shows the photoelectric opacity as a function of energy together with the Thomson opacity, while the right panel shows the resulting transmitted spectra. Even at the highest ionization predicted by our estimates of the warm corona, the original blackbody spectrum (dashed line) is severely modified by photoelectric absorption.

They found that despite the very high ionization at the center of the cloud, in the outer parts ions such as Fe XXII were still dominant, producing distinct spectral features.

As before, we use the XSTAR code to test this scenario by producing the solution for a plasma under photoionization equilibrium (PIE) using the estimates shown above; i.e., $\xi \sim 10^6 \, \mathrm{erg\,cm\,s^{-1}}$, $n_\mathrm{e} = 10^{12} \, \mathrm{cm^{-3}}$, and $N_\mathrm{H} = 10^{25} \, \mathrm{cm^2}$. Using a blackbody with $kT = 0.1 \, \mathrm{keV}$ as the input spectrum, the resulting gas temperature is $T \sim 10^6 \, \mathrm{K}$. Despite the large ionization, the photoelectric opacity near $1 \, \mathrm{keV}$ is still dominant (or at least comparable) to the Thompson opacity (left panel in Figure 6). We repeated this calculation by raising the ionization to the largest value predicted by Equation 7 (i.e., $\xi \sim 10^9 \, \mathrm{erg\,cm\,s^{-1}}$), but the net effect is small in reducing the photoelectric opacity. Just as in the case of CIE, the transmitted spectra show strong absorption features in the observable bandpass (right panel in Figure 6). Despite the large ionizing flux, the input spectrum is too soft to fully ionize the metals in the gas.

None of the spectra resulting from either the CIE or PIE simulations are likely to resemble the apparently featureless broad component required to fit the soft excess. In the case of PIE, a harder spectrum extending to high energies is likely to provide enough photons to fully ionize the medium, such as that provided by the hot corona. However, strong photoionization will raise the temperature and can only fully ionize the atmosphere if the optical depth is much smaller than that inferred from fitting the warm corona model. Moreover, strong illumination of an optically-thick medium is expected to produce strong reprocessing of the photons, which is a situation that closely resembles the relativistic reflection

model. This alternative scenario is discussed in the next Section.

4.2. Implications of the Relativistic Reflection Model

The relativistic reflection model has also been proposed as a possible explanation for the soft excess in AGN. When strong radiation is produced in the central region close the black hole, the reprocessing of the hard X-rays in the optically thick and relatively cold accretion disk is an expected consequence. If the reflection occurs close enough to the horizon, the relativistic effects will distort the spectrum, broadening and skewing all the spectral features. Below $\sim 1 \, \mathrm{keV}$, a rich forest of fluorescence emission lines produced by ions with nuclear charge lower than iron is predicted (e.g., Ross & Fabian 2005; García & Kallman 2010). When the gravitational blurring is extreme, these features will blend creating a single broad and smooth excess at soft energies. When facing the difficulties in making physical sense out of a featureless and broad spectrum emitted from a warm corona, a relativistically blurred reflection spectrum provides an alternative and somewhat more consistent interpretation. However, some caveats must also be considered when adopting this model. Below we discuss this scenario to explain the soft excess in Mrk 509.

In their analysis of a sample of 25 "bare" AGN with *Suzaku*, Walton et al. (2013) fitted $\sim 90 \, \mathrm{ks}$ XIS/PIN spectra of Mrk 509 using a model consisting of ionized and relativistic plus neutral and distant reflection components. Both components were modeled with `reflionx` (Ross & Fabian 2005). A warm absorber component was also included and modeled with XSTAR. The relativistic blurring applied to the ionized reflection em-

ployed `relconv` (Dauser et al. 2013). Two sets of fits were performed: one with a fixed cross-normalization constant between the hard X-ray PIN and the soft X-ray XIS detectors, and another in which this cross-normalization $C_{\rm PIN/XIS}$ was allowed to vary. The uncertainty introduced by $C_{\rm PIN/XIS}$ has critical impact on the results for Mrk 509. In short, two vastly different pictures emerge from the fits, simply due to differences in the hard X-ray component. In the first instance of fixed $C_{\rm PIN/XIS} = 1.17$, the system demands a high spin $a = 0.86 \pm 0.02$ and face-on orientation (inclination of $i < 18°$). However, when $C_{\rm PIN/XIS}$ is freed, it becomes loosely constrained ($C_{\rm PIN/XIS} < 1.06$), while spin and inclination are drastically affected: $a = 0.36 \pm 0.3$ and $i = 50 \pm 5°$. This is because the hard X-ray band is essential for disentangling the power-law continuum from the ionized reflection component, which motivated the *NuSTAR* observations presented here.

The fit described in Section 3.2 and shown in Figure 4 demonstrates that the relativistic reflection scenario (Model 2) provides a good description of the present *Suzaku* and *NuSTAR* data for Mrk 509, with results that are broadly consistent with the high-spin fits presented by Walton et al. (2013). Moreover, our fits have been carried out with updated reflection models, which include more complete atomic data, improved radiative transfer calculations, and the possibility for higher densities in the reflector. This latter improvement is important to better describe the soft excess observed below 1 keV.

It is worth noticing the relevance of the *NuSTAR* data in providing high signal-to-noise data at hard energies, where most of the reflection signatures are observed. This is particularly important because not only our *Suzaku* exposure is shorter than that analyzed by Walton et al. (2013), but also because our data lack the high-energy coverage previously provided by the PIN instrument (not longer operational in the last *Suzaku* cycle). In the case of the relativistic reflection Model 2, fitting the *Suzaku* data alone yield poor constraints to important parameters such as spin ($a_* > 0.702$), coronal height ($h = 2.01^{+0.29}_{-2.74} R_{\rm Hor}$), and inclination ($i = 51.4 \pm 8°$). Unsurprisingly, the disk density is determined with a similar uncertainty ($\log n_{\rm e}/{\rm cm}^{-3} > 18$), as this parameter is mostly sensitive to the soft-energy data.

When applied to both the *Suzaku* and *NuSTAR* data, the goodness-of-fit for the relativistic reflection model ($\chi^2_\nu = 1.054$) is very similar to that from the fits with the warm corona picture ($\chi^2_\nu = 1.049$, Model 1.3). The similarity between the warm corona and the relativistic reflection model has also been previously discussed by

Boissay et al. (2014). In Figure 7 we show these two models overplotted with the observed data. It is clear that the two models are almost identical in the energy band considered for the fits (1–79 keV), which is shown with the shaded regions. We emphasize that data below 1 keV was excluded given concerns in the calibration of *Suzaku*'s instruments in this band towards the end the mission (see Section 2.3). We note, however, that when these data are included (without refitting), they seem to favor the trend predicted by the relativistic reflection model. Nevertheless, the lack reliable data below 1 keV limits the analysis of the present study, as we cannot fully constrain the overall shape of the soft excess. Thus, future observations with sensitive coverage of both the soft and hard energy bands will become crucial to further understand the nature of the soft excess in Mrk 509, and several other AGN.

The small differences between the two models seen at high energies ($\sim 30 - 50$ keV, Figure 7), are likely due to the fact that the reflection models used here were calculated with a cutoff energy fixed at 300 keV, while in the warm corona fit this parameter is allowed to vary freely. This suggests that a lower coronal temperature would be possible with the reflection model, but it is probably not very well constrained, as it does not seem to affect the fit statistics significantly.

The relativistic reflection model requires a large value for the black hole spin (consistent with its maximum value, $a_* > 0.993$), and low coronal height ($h = 1.53^{+0.01}_{-0.25} R_{\rm Hor}$). While high spins and compact coronae are commonly reported for AGN, a corona placed so close to the black hole implies a very extreme configuration in which most of the radiation is focused toward the disk due to the strong light bending (Dauser et al. 2016). This configuration predicts a reflection-dominated spectrum, different to the fit achieved with Model 2 (Figure 4, right). Nonetheless, modeling the primary source of X-rays as a point source in the rotational axis is a rather simple and idealized description, and thus the derived parameters need to be interpreted with care.

The iron abundance is found to be close to its Solar value ($A_{\rm Fe} < 0.82$). Fixing $A_{\rm Fe} = 1$ worsens the fit by $\Delta\chi^2 \sim 12$, having no obvious effect on the rest of the model parameters. While Solar abundances are the canonical expectation, much larger Fe abundances are commonly derived from reflection modeling (García et al. 2018). However, recent studies indicate that high-density reflection models (like the ones used here) lead to abundances closer to Solar (e.g.; Tomsick et al. 2018; Jiang et al. 2018), which is consistent with our findings. Moreover, visual inspection of the residuals reveals no

obvious signs of iron emission lines after the distant reflection is accounted for (e.g., see Figure 3), suggesting that the reflection spectrum is primarily constrained by fitting the soft-excess.

The large density of the accretion disk derived from our fits ($\log n_{\mathrm{e}}/\mathrm{cm}^{-3} > 18.2$) also places this source in a somewhat extreme configuration. For instance, Svensson & Zdziarski (1994) derived analytic expressions for a hot corona around a cold α-disk system. Using their expression for the disk density in the radiation-pressure-dominated case (i.e., their Equation 8)

$$n_{\mathrm{e}} = \frac{1}{\sigma_{\mathrm{T}} R_{\mathrm{S}}} \frac{256\sqrt{2}}{27} \alpha^{-1} r^{3/2} \dot{m}^{-2} \left[1 - (3/r)\right]^{-1} (1-f)^{-3}. \tag{8}$$

where $\alpha \approx 0.1$ is the standard Shakura & Sunyaev (1973) dimensionless parameter connecting the viscosity with the gas pressure, $r = 10$ is the radius in units of $R_{\mathrm{S}} = 2R_g$, $\dot{m} = 0.1$, $n_{\mathrm{e}} = 10^{19}\,\mathrm{cm}^{-3}$, and f is the fraction of the total accretion power dissipated by the corona. We find $f = 0.86$, which means that most of the accretion power needs to be dissipated in the hot corona. We note that more conservative values can be found in the literature. For example, Vasudevan & Fabian (2007) reported $f \sim 0.11 - 0.45$ for a sample of 54 AGN. Nevertheless, our estimate for Mrk 509, albeit extreme, is allowed within the applicability regime of the hot corona and cold disk model.

Meanwhile, high-density reflection models like the one used here have recently been used to successfully describe the spectrum of the AGN IRAS 13224−3809 (Parker et al. 2017; Jiang et al. 2018), and Mrk 1044 (Mallick et al. 2018), as well as of the black hole binary Cyg X-1 (Tomsick et al. 2018). In all these cases, fitting the observed soft excess results in a lower (and more physical) iron abundance in the reflector (see also discussion in Parker et al. 2018). However, in the case of Ark 120, Porquet et al. (2018) find that the warm corona model provides a better description of the data over the relativistic reflection picture, even when high-density models were tested. In a multi-epoch study of Mrk 335, Keek & Ballantyne (2016) showed that after fitting reflection above 3 keV, a constant soft excess appears to remain that is constant to the flux of the source. However, they have only used standard relativistic reflection, as the high-density reflection models like the ones used here were not available at the time.

One argument against the relativistic reflection scenario (and consequently in favor of the warm corona picture), on the other hand, is the apparent discrepancy in the correlation between the strengths of the reflection (R_{f}) and the soft excess (R_{SE}) components predicted by relativistic reflection models and that observed in
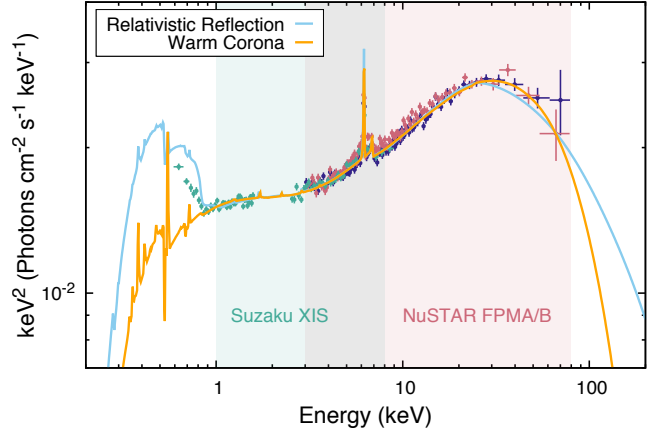
Figure 7. Unfolded spectra of Mrk 509 as seen by *Suzaku* XIS and *NuSTAR* FPMA and FPMB (data points), together with the two different scenarios for the soft excess (solid lines), the relativistic reflection (Model 2), and the warm corona (Model 1.3). The shaded regions show the data from each instrument that was included in the fits.

Seyfert AGN. Boissay et al. (2016) showed that while simulations with reflection models predict a positive correlation between R_{f} and R_{SE} (see also Vasudevan et al. 2014), observations of a sample of 42 AGN show a negative correlation. They argued that this discrepancy can be overcome if instead the soft excess is modeled with warm Comptonization models. However, their sample includes data that are not simultaneous, which is likely to bias their results for sources with strong variability. More importantly, their fits implement very simplistic models for reflection, which are fundamentally incorrect to properly describe the combination of distant (non-relativistic) and local (relativistic) reflection. In many un-obscured AGN, the narrow (unblurred) reflection component dominates the relativistic reflection signal (e.g., Ricci et al. 2014). Thus, the reflection fraction measured by Boissay et al. (2016) is likely biased towards the strength of the distant reflector. In this case, the anti-correlation with the strength of the soft excess can be simply explained by geometrical effects. For sources that are more obscured, the emission from the inner-most regions will tend to be reduced, which reduces the direct continuum (increasing R_{f}) as well as the local relativistic reflection component (decreasing R_{SE}).

5. CONCLUSIONS

We have presented an analysis of the X-ray spectrum (1–79 keV) of the bright Seyfert 1 AGN Mrk 509. These data, obtained during April–June 2015 with *Suzaku* and *NuSTAR* reveal signatures of X-ray reprocessing from an optically thick and relatively cold material, a power-law continuum, and a strong soft excess. By perform-

ing fits of different modern models, we have shown that these data can be described by a hot corona which produces the power-law continuum (modeled with a standard Comptonization model), and a distant reflection from a cold material (which can be described with a variety of reflection models). Meanwhile, the soft excess can be fitted with either a warm Comptonizing corona, or with a relativistically blurred high-density reflection model. These two prescriptions imply two very different interpretations of the observed spectrum, and they cannot be easily distinguished on statistical grounds alone. Although the *Suzaku* data below $1\,\text{keV}$ seems to favor the relativistic reflection scenario, this energy range was excluded from the fit due to concerns regarding the quality of the instrumental calibration.

Since no model can be preferred based on the fit statistics, we have discussed in detail the physical implications of these two models. In particular, we find that the quantities required to fit the soft excess with the warm corona model—i.e., low temperature ($kT \sim 0.5 - 1\,\text{keV}$) and large optical depth ($\tau_{\text{T}} \sim 10 - 20$)— are incompatible with the physical concept of a corona, in which electron scattering is expected to be the dominant source of opacity. Using simple estimates of density, flux, and ionization parameter, we have carried out calculations of plasmas in coronal and photoionization equilibrium. In both cases, we found that atomic opacities will dominate over Thomson opacities, predicting very strong absorption features in the observed spectrum. Taking these simulations to the most extreme cases, we find that it is very unlikely that a warm corona can produce the soft featureless emission required to fit the data.

On the other hand, the relativistic reflection model appears more reasonable on physical grounds. Signatures of X-ray reflection have been shown to be almost ubiquitous in most Seyfert AGN spectra, and thus it is also expected to be present in Mrk 509. The relativistic reflection model requires extreme values for the spin and coronal compactness, as well as a very large density for the reflector. Although large densities are somewhat unexpected in accretion disks around supermassive black holes, we cannot discard this possibility. Therefore, based on the analysis presented here, we favor the high-density relativistic reflection scenario to explain the soft excess in Mrk 509.

Nonetheless, the present discussion is not entirely conclusive. The calculations described above do not include photon redistribution due to Comptonization in the medium, nor any other source of turbulent motions capable to broaden and smear the absorption lines present in the spectra. Evidently, these effects are only relevant for the simulations at the highest temperatures

($T \sim 10^7\,\text{K}$). For lower temperatures, the drastic modification of the spectrum due to the strong absorption prevents this model to reproduce the soft excess. Detailed radiative transfer calculations covering larger optical depths, Comptonization, velocity components, and the effects of the response of current instruments are necessary to fully explore this problem. Such calculations are well outside the scope of the present work, and thus will be featured in a future publication.

Finally, deeper observations of this source should be able to confirm or not the presence of relativistic reflection. To clearly distinguish between the narrow and broad components, future missions flying microcalorimeters such as *XRISM* (Tashiro et al. 2018), *Athena* (Nandra et al. 2013), and *Lynx* (Özel 2018), will become crucial. However, in order to detect the shift of Compton hump between the relativistic and the non-relativistic reflection, focusing of hard photons with larger effective area than *NuSTAR* is necessary. The concept mission *HEX-P* (Madsen et al. 2018), will offer these capabilities. Likewise, observations with instruments with broad-band coverage and good sensitivity to both low and energies such as *STROBE-X* (Ray et al. 2018) will help to break model degeneracies further understand the nature of the soft excess in Mrk 509 and many other AGN.

Facilities: NuSTAR, Suzaku (XIS)

Software: XSPEC (v12.9.0d; Arnaud 1996), MYTORUS (Murphy & Yaqoob 2009), BORUS02 (Baloković et al. 2018), XILLVER (García & Kallman 2010; García et al. 2013), RELX-ILL (v1.2.0; García et al. 2014; Dauser et al. 2014), XSTAR (v2.41; Kallman & Bautista 2001), NUSTRADAS (v1.6.0)

REFERENCES

Arnaud, K. A. 1996, in Astronomical Society of the Pacific Conference Series, Vol. 101, Astronomical Data Analysis Software and Systems V, ed. G. H. Jacoby & J. Barnes, 17

Arnaud, K. A., Branduardi-Raymont, G., Culhane, J. L., et al. 1985, MNRAS, 217, 105, doi: 10.1093/mnras/217.1.105

Baloković, M., Matt, G., Harrison, F. A., et al. 2015, ApJ, 800, 62, doi: 10.1088/0004-637X/800/1/62

Baloković, M., Brightman, M., Harrison, F. A., et al. 2018, ApJ, 854, 42, doi: 10.3847/1538-4357/aaa7eb

Boissay, R., Ricci, C., & Paltani, S. 2016, A&A, 588, A70, doi: 10.1051/0004-6361/201526982

Boissay, R., Paltani, S., Ponti, G., et al. 2014, A&A, 567, A44, doi: 10.1051/0004-6361/201423494

Brenneman, L. W., Madejski, G., Fuerst, F., et al. 2014, ApJ, 788, 61, doi: 10.1088/0004-637X/788/1/61

Brightman, M., & Nandra, K. 2011, MNRAS, 413, 1206, doi: 10.1111/j.1365-2966.2011.18207.x

Cappi, M., Tombesi, F., Bianchi, S., et al. 2009, A&A, 504, 401, doi: 10.1051/0004-6361/200912137

Costantini, E., Kriss, G., Kaastra, J. S., et al. 2016, A&A, 595, A106, doi: 10.1051/0004-6361/201527956

Crummy, J., Fabian, A. C., Gallo, L., & Ross, R. R. 2006, MNRAS, 365, 1067, doi: 10.1111/j.1365-2966.2005.09844.x

Czerny, B., & Elvis, M. 1987, ApJ, 321, 305, doi: 10.1086/165630

Czerny, B., Nikołajuk, M., Różańska, A., et al. 2003, A&A, 412, 317, doi: 10.1051/0004-6361:20031441

Dauser, T., García, J., Parker, M., Fabian, A., & Wimls, J. 2014, Submitted to MNRAS, 430, 1694

Dauser, T., García, J., Walton, D. J., et al. 2016, A&A, 590, A76, doi: 10.1051/0004-6361/201628135

Dauser, T., Garcia, J., Wilms, J., et al. 2013, MNRAS, 430, 1694, doi: 10.1093/mnras/sts710

Done, C., Davis, S. W., Jin, C., Blaes, O., & Ward, M. 2012, MNRAS, 420, 1848, doi: 10.1111/j.1365-2966.2011.19779.x

Fabian, A. C., Ballantyne, D. R., Merloni, A., et al. 2002, MNRAS, 331, L35, doi: 10.1046/j.1365-8711.2002.05419.x

Fabian, A. C., Zoghbi, A., Ross, R. R., et al. 2009, Nature, 459, 540, doi: 10.1038/nature08007

Fisher, K. B., Huchra, J. P., Strauss, M. A., et al. 1995, ApJS, 100, 69, doi: 10.1086/192208

García, J., Dauser, T., Reynolds, C. S., et al. 2013, ApJ, 768, 146, doi: 10.1088/0004-637X/768/2/146

García, J., & Kallman, T. R. 2010, ApJ, 718, 695, doi: 10.1088/0004-637X/718/2/695

García, J., Dauser, T., Lohfink, A., et al. 2014, ApJ, 782, 76, doi: 10.1088/0004-637X/782/2/76

García, J. A., Dauser, T., Steiner, J. F., et al. 2015, ApJL, 808, L37, doi: 10.1088/2041-8205/808/2/L37

García, J. A., Fabian, A. C., Kallman, T. R., et al. 2016, MNRAS, 462, 751, doi: 10.1093/mnras/stw1696

García, J. A., Kallman, T. R., Bautista, M., et al. 2018, in Astronomical Society of the Pacific Conference Series, Vol. 515, 282

George, I. M., & Fabian, A. C. 1991, MNRAS, 249, 352

Gierliński, M., & Done, C. 2004, MNRAS, 349, L7, doi: 10.1111/j.1365-2966.2004.07687.x

Haardt, F. 1993, ApJ, 413, 680, doi: 10.1086/173036

Harrison, F. A., Craig, W. W., Christensen, F. E., et al. 2013, ApJ, 770, 103, doi: 10.1088/0004-637X/770/2/103

Jiang, J., Parker, M. L., Fabian, A. C., et al. 2018, MNRAS, 477, 3711, doi: 10.1093/mnras/sty836

Jin, C., Done, C., Ward, M., Gierliński, M., & Mullaney, J. 2009, MNRAS, 398, L16, doi: 10.1111/j.1745-3933.2009.00697.x

Kaastra, J. S., Petrucci, P.-O., Cappi, M., et al. 2011, A&A, 534, A36, doi: 10.1051/0004-6361/201116869

Kaastra, J. S., Ebrero, J., Arav, N., et al. 2014, A&A, 570, A73, doi: 10.1051/0004-6361/201424662

Kalberla, P. M. W., Burton, W. B., Hartmann, D., et al. 2005, A&A, 440, 775, doi: 10.1051/0004-6361:20041864

Kallman, T., & Bautista, M. 2001, ApJS, 133, 221, doi: 10.1086/319184

Kara, E., García, J. A., Lohfink, A., et al. 2017, MNRAS, 468, 3489, doi: 10.1093/mnras/stx792

Kaufman, J., Blaes, O. M., & Hirose, S. 2018, MNRAS, 476, 5548, doi: 10.1093/mnras/sty540

Keck, M., Brenneman, L., Ballantyne, D., et al. 2014

Keek, L., & Ballantyne, D. R. 2016, MNRAS, 456, 2722, doi: 10.1093/mnras/stv2882

Kettula, K., Nevalainen, J., & Miller, E. D. 2013, A&A, 552, A47, doi: 10.1051/0004-6361/201220408

Koyama, K., Tsunemi, H., Dotani, T., et al. 2007, PASJ, 59, 23, doi: 10.1093/pasj/59.sp1.S23

Krolik, J. H., & Kallman, T. R. 1984, ApJ, 286, 366, doi: 10.1086/162608

Laor, A. 1991, ApJ, 376, 90, doi: 10.1086/170257

Leighly, K. M. 1999, ApJS, 125, 317, doi: 10.1086/313287

Liu, Y., & Li, X. 2015, MNRAS, 448, L53, doi: 10.1093/mnrasl/slu198

Madsen, K. K., Beardmore, A. P., Forster, K., et al. 2017, AJ, 153, 2, doi: 10.3847/1538-3881/153/1/2

Madsen, K. K., Harrison, F. A., Markwardt, C. B., et al. 2015, ApJS, 220, 8, doi: 10.1088/0067-0049/220/1/8

Madsen, K. K., Harrison, F., Broadway, D., et al. 2018, in Society of Photo-Optical Instrumentation Engineers (SPIE) Conference Series, Vol. 10699, Society of Photo-Optical Instrumentation Engineers (SPIE) Conference Series, 106996M

Magdziarz, P., Blaes, O. M., Zdziarski, A. A., Johnson, W. N., & Smith, D. A. 1998, MNRAS, 301, 179, doi: 10.1046/j.1365-8711.1998.02015.x

Mallick, L., Alston, W. N., Parker, M. L., et al. 2018, MNRAS, 479, 615, doi: 10.1093/mnras/sty1487

Marinucci, A., Bianchi, S., Braito, V., et al. 2018, MNRAS, 478, 5638, doi: 10.1093/mnras/sty1436

Marinucci, A., Tortosa, A., & NuSTAR AGN Physics Working Group. 2016, Astronomische Nachrichten, 337, 490, doi: 10.1002/asna.201612335

Markoff, S., Nowak, M. A., & Wilms, J. 2005, 635, 1203

Matt, G., Perola, G. C., & Piro, L. 1991, A&A, 247, 25

Matt, G., Perola, G. C., Piro, L., & Stella, L. 1992, A&A, 257, 63

Mehdipour, M., Branduardi-Raymont, G., Kaastra, J. S., et al. 2011, A&A, 534, A39, doi: 10.1051/0004-6361/201116875

Middleton, M., Done, C., Ward, M., Gierliński, M., & Schurch, N. 2009, MNRAS, 394, 250, doi: 10.1111/j.1365-2966.2008.14255.x

Miniutti, G., Ponti, G., Greene, J. E., et al. 2009, MNRAS, 394, 443, doi: 10.1111/j.1365-2966.2008.14334.x

Morini, M., Lipani, N. A., & Molteni, D. 1987, ApJ, 317, 145, doi: 10.1086/165262

Murphy, K. D., & Yaqoob, T. 2009, MNRAS, 397, 1549, doi: 10.1111/j.1365-2966.2009.15025.x

Nandra, K., Barret, D., Barcons, X., et al. 2013, ArXiv e-prints, arXiv:1306.2307. https://arxiv.org/abs/1306.2307

Nardini, E., Fabian, A. C., & Walton, D. J. 2012, MNRAS, 423, 3299, doi: 10.1111/j.1365-2966.2012.21123.x

Nardini, E., Porquet, D., Reeves, J. N., et al. 2016, ApJ, 832, 45, doi: 10.3847/0004-637X/832/1/45

Özel, F. 2018, Nature Astronomy, 2, 608, doi: 10.1038/s41550-018-0548-3

Parker, M. L., Miller, J. M., & Fabian, A. C. 2018, MNRAS, 474, 1538, doi: 10.1093/mnras/stx2861

Parker, M. L., Pinto, C., Fabian, A. C., et al. 2017, Nature, 543, 83, doi: 10.1038/nature21385

Peterson, B. M., Ferrarese, L., Gilbert, K. M., et al. 2004, ApJ, 613, 682, doi: 10.1086/423269

Petrucci, P. O., Merloni, A., Fabian, A., Haardt, F., & Gallo, E. 2001, MNRAS, 328, 501, doi: 10.1046/j.1365-8711.2001.04897.x

Petrucci, P.-O., Ursini, F., De Rosa, A., et al. 2018, A&A, 611, A59, doi: 10.1051/0004-6361/201731580

Petrucci, P.-O., Paltani, S., Malzac, J., et al. 2013, A&A, 549, A73, doi: 10.1051/0004-6361/201219956

Piconcelli, E., Jimenez-Bailón, E., Guainazzi, M., et al. 2005, A&A, 432, 15, doi: 10.1051/0004-6361:20041621

Ponti, G., Cappi, M., Costantini, E., et al. 2013, A&A, 549, A72, doi: 10.1051/0004-6361/201219450

Porquet, D., Reeves, J. N., O'Brien, P., & Brinkmann, W. 2004, A&A, 422, 85, doi: 10.1051/0004-6361:20047108

Porquet, D., Reeves, J. N., Matt, G., et al. 2018, A&A, 609, A42, doi: 10.1051/0004-6361/201731290

Pounds, K. A., Nandra, K., Fink, H. H., & Makino, F. 1994, MNRAS, 267, 193

Pounds, K. A., Warwick, R. S., Culhane, J. L., & de Korte, P. A. J. 1986, MNRAS, 218, 685, doi: 10.1093/mnras/218.4.685

Ray, P. S., Arzoumanian, Z., Brandt, S., et al. 2018, in Society of Photo-Optical Instrumentation Engineers (SPIE) Conference Series, Vol. 10699, Society of Photo-Optical Instrumentation Engineers (SPIE) Conference Series, 1069919

Ricci, C., Ueda, Y., Paltani, S., et al. 2014, MNRAS, 441, 3622, doi: 10.1093/mnras/stu735

Ricci, C., Trakhtenbrot, B., Koss, M. J., et al. 2017, ApJS, 233, 17, doi: 10.3847/1538-4365/aa96ad

Risaliti, G., Harrison, F. A., Madsen, K. K., et al. 2013, Nature, 494, 449, doi: 10.1038/nature11938

Ross, R. R., & Fabian, A. C. 2005, MNRAS, 358, 211, doi: 10.1111/j.1365-2966.2005.08797.x

Ross, R. R., Weaver, R., & McCray, R. 1978, ApJ, 219, 292, doi: 10.1086/155776

Różańska, A., Malzac, J., Belmont, R., Czerny, B., & Petrucci, P.-O. 2015, A&A, 580, A77, doi: 10.1051/0004-6361/201526288

Shakura, N. I., & Sunyaev, R. A. 1973, å, 24, 337

Singh, K. P., Garmire, G. P., & Nousek, J. 1985, ApJ, 297, 633, doi: 10.1086/163560

Smith, R. A. N., Page, M. J., & Branduardi-Raymont, G. 2007, A&A, 461, 135, doi: 10.1051/0004-6361:20065348

Svensson, R., & Zdziarski, A. A. 1994, ApJ, 436, 599, doi: 10.1086/174934

Tashiro, M., Maejima, H., Toda, K., et al. 2018, in Society of Photo-Optical Instrumentation Engineers (SPIE) Conference Series, Vol. 10699, 1069922

Tomsick, J. A., Parker, M. L., García, J. A., et al. 2018, ApJ, 855, 3, doi: 10.3847/1538-4357/aaaab1

Tortosa, A., Bianchi, S., Marinucci, A., Matt, G., & Petrucci, P. O. 2018, A&A, 614, A37, doi: 10.1051/0004-6361/201732382

Tortosa, A., Marinucci, A., Matt, G., et al. 2017, MNRAS, 466, 4193, doi: 10.1093/mnras/stw3301

Ursini, F., Boissay, R., Petrucci, P.-O., et al. 2015, A&A, 577, A38, doi: 10.1051/0004-6361/201425401

Vasudevan, R. V., & Fabian, A. C. 2007, MNRAS, 381, 1235, doi: 10.1111/j.1365-2966.2007.12328.x

Vasudevan, R. V., Mushotzky, R. F., Reynolds, C. S., et al. 2014, ApJ, 785, 30, doi: 10.1088/0004-637X/785/1/30

Vaughan, S., Edelson, R., Warwick, R. S., & Uttley, P. 2003, MNRAS, 345, 1271, doi: 10.1046/j.1365-2966.2003.07042.x

Verner, D. A., Ferland, G. J., Korista, K. T., & Yakovlev, D. G. 1996, ApJ, 465, 487, doi: 10.1086/177435

Walter, R., & Fink, H. H. 1993, A&A, 274, 105

Walton, D. J., Nardini, E., Fabian, A. C., Gallo, L. C., & Reis, R. C. 2013, MNRAS, 428, 2901, doi: 10.1093/mnras/sts227

Walton, D. J., Risaliti, G., Harrison, F. A., et al. 2014, ApJ, 788, 76, doi: 10.1088/0004-637X/788/1/76

Walton, D. J., Tomsick, J. A., Madsen, K. K., et al. 2016, ApJ, 826, 87, doi: 10.3847/0004-637X/826/1/87

Wilms, J., Allen, A., & McCray, R. 2000, ApJ, 542, 914, doi: 10.1086/317016

Woo, J.-H., & Urry, C. M. 2002, ApJ, 579, 530, doi: 10.1086/342878

Xu, Y., Baloković, M., Walton, D. J., et al. 2017, ApJ, 837, 21, doi: 10.3847/1538-4357/aa5df4

Yaqoob, T., Murphy, K. D., Griffiths, R. E., et al. 2007, PASJ, 59, 283

Zdziarski, A. A., Johnson, W. N., & Magdziarz, P. 1996, MNRAS, 283, 193, doi: 10.1093/mnras/283.1.193

Życki, P. T., Done, C., & Smith, D. A. 1999, MNRAS, 309, 561, doi: 10.1046/j.1365-8711.1999.02885.x